EARTHARXIV PREPRINT • VERSION 1 • NON-PEER-REVIEWED

Adalar at the Eastern Marmara Seismic Gap: The August 2026 Earthquake Cluster and Its Implications for Seismic Hazard near Istanbul

Integrated geotectonic, geophysical and geotechnical assessment with Figures S2–S11

Shaheen Mohammed Saleh Ahmed • ORCID: https://orcid.org/0000-0002-9289-128X

1 Department of Geology, College of Science, Kirkuk University, Kirkuk 36001, Iraq

2 Department of Geology, Faculty of Engineering, Çukurova University, Balcalı, Adana 01330, Türkiye

Corresponding author: shaheen1965@uokirkuk.edu.iq

EarthArXiv preprint status

This manuscript is a non-peer-reviewed preprint submitted to EarthArXiv.

Journal status: not submitted to a peer-reviewed journal at the time of Version 1.

Scope and cutoff: the analysis covers 1 August 2026 00:00 UTC to 20 August 2026 10:18:27 UTC. The final day is incomplete, and agency solutions may be revised.

Scientific caution: the hotspot, ellipse, relocation, focal-mechanism, Coulomb, and geotechnical results are screening interpretations. They are not an earthquake prediction.

Preprint Version 1 • 20 August 2026

Abstract

The eastern Marmara Sea and Adalar sector lie close to İstanbul and the western North Anatolian Fault, where earthquake-source processes interact with strong basin and site effects. This study integrates a reconciled earthquake catalog, waveform-quality measures, spatial statistics, trial hypocentral relocation, reconnaissance focal mechanisms, point-source Coulomb stress screening, and published engineering-geological evidence for 1–20 August 2026. The catalog contains 127 regional events, including 79 events within 40 km of Adalar. Sixty-two of the Adalar-window events occurred on 19–20 August, and the largest event was ML 3.2 at a reported depth of 7 km. A 10-km spatial neighborhood produced the strongest standardized Moran result (z = 21.69), and 13 cells remained in the 99% Getis–Ord Gi* hot class after false-discovery-rate correction. Bootstrap standard deviational ellipses confirm an elongated distribution but do not define a rupture plane. The waveform archive contains 549 automatic P picks from 49 stations; however, 547 picks are from one network, and only four automatic picks were retained for the ML 3.2 event. Twelve of 22 trial relocations passed permissive gates, but only four satisfied a stricter joint 10-km horizontal and depth-uncertainty criterion. The focal-mechanism sample is too sparse and dispersed to define a new Adalar stress tensor, so the published regional maximum compression near N35°E remains the most defensible first-order constraint. A point-source model for the 23 April 2025 Mw 6.2 event gives a small positive median Coulomb stress change of +0.204 kPa in the Çınarcık receiver corridor; this does not demonstrate triggering. The combined evidence supports denser offshore monitoring, reviewed phase picking, improved relocation, and site-specific geotechnical investigation. It does not predict the time, magnitude, or location of a future earthquake.

Keywords: Marmara Sea; Adalar; North Anatolian Fault; earthquake clustering; Getis–Ord Gi*; Coulomb stress; site response; seismic-hazard screening

Central interpretation
The August 2026 sequence increases the need for dense Adalar monitoring and better site characterization. It does not predict the time, magnitude or exact location of a future damaging earthquake.

Table 1. Main quantitative findings.

Component	Result	Scientific meaning
Regional catalog	127 events; M 0.9–3.4	Short observational window
Adalar window	79 events within 40 km	12 events M≥2.5
Late sequence	62 events on 19–20 Aug	78.5% of Adalar total
Largest Adalar event	ML 3.2; depth 7.0 km	19 Aug 14:43:46 UTC
Hotspot neighborhood	10 km; Moran z=21.69	13 FDR-controlled 99% hot cells
Automatic picks	549 picks; 49 stations	547 from KO network
Relocations	12/22 pass notebook gates	Only 4 pass strict 10×10 km uncertainty check
Focal directions	Axial R≈0.20	Insufficient for a new Adalar stress inversion
Published stress	Regional σ1/SHmax≈N35°E	First-order literature constraint
Çınarcık Coulomb median	+0.204 kPa	Small, point-source and model dependent

Note. *All values refer to the supplied version at the stated cutoff. None is a time-dependent earthquake probability.*

1. Introduction and study scope

The purpose of this report is to explain Supplementary Figures S2–S11 in simple academic language and to connect the results with engineering and tectonic knowledge of the Marmara region. Three questions are addressed: (1) What does the August 2026 sequence show about present seismic activity? (2) What can be learned about fault geometry, stress and monitoring quality? (3) What are the correct geotechnical implications for coastal settlements, infrastructure and future site investigation?

The report does not provide a probabilistic seismic-hazard calculation, a code-based design spectrum or a building-safety certificate. It also does not replace geotechnical investigation. The spatial scores, ellipses and Coulomb values are screening tools. Their purpose is to organize observations and identify where better measurements are needed.

2. Geological and geotectonic setting

2.1 Main Marmara Fault and basin architecture

The Marmara Sea lies on the western North Anatolian Fault, a major right-lateral plate-boundary fault. The offshore fault is commonly called the Main Marmara Fault. It crosses a complex system of basins and structural highs, including the Tekirdağ, Central, Kumburgaz and Çınarcık domains. Detailed marine mapping shows that the system is segmented and includes bends, stepovers and secondary structures rather than one perfectly uniform fault plane (Le Pichon et al., 2001). This geometry can influence where earthquakes start, how ruptures propagate and where they stop.

The eastern Marmara sector is especially important because it lies close to İstanbul and Adalar. Borehole seismology identified a low-seismicity patch south of İstanbul that extends to about 10 km depth and has been interpreted as a locked fault section (Bohnhoff et al., 2013). Geodetic studies also show important strain accumulation along parts of the central and eastern system (Ergintav et al., 2014; Lange et al., 2019). In contrast, repeating earthquakes and seafloor measurements show partial creep in some western and central sections (Yamamoto et al., 2019; Becker et al., 2023).

2.2 Adalar sector and present tectonic concern

Adalar is located near the eastern end of the offshore seismic gap and close to the transition toward the 1999 İzmit rupture system. Recent work has increased concern about eastward rupture interaction. Chen et al. (2025) found mainly eastward directivity for a set of moderate MMF earthquakes west of the Princes Islands. Martínez-Garzón et al. (2026) interpreted recent M>5 ruptures, including the 2025 Mw 6.2 earthquake, as a progressive eastward sequence. These results support strong monitoring, but they do not provide a short-term prediction.

Physics-based studies show why simple prediction is not possible. Non-planar fault geometry, stress heterogeneity and crustal rheology can produce rupture arrest, segment-to-segment transfer or larger cascading rupture (Korkusuz Öztürk et al., 2025; Güvercin & Barbot, 2025; Fernandez et al., 2026). Therefore, the August event cluster must be interpreted within several possible tectonic scenarios.

3. Data and methods

3.1 Catalog acquisition and reconciliation

Earthquake origins and magnitudes were queried independently from AFAD, EMSC, and USGS for the Marmara study region. AFAD was used as the preferred local solution when available. Solutions were associated when origin times differed by no more than 15 s and epicentres by no more than 25 km. Alternative agency identifiers and magnitudes were retained. The resulting short-window catalog contains 127 regional events; an Adalar subset was defined by a 40-km radius. The 20 August window is incomplete and is treated as a provisional cutoff.

3.2 Waveforms, phase picks and trial relocation

Station metadata and waveforms were obtained through FDSN/EIDA services for networks and stations surrounding the Marmara Sea. Automatic P arrivals were retained only after signal and uncertainty gates. Trial locations used a robust one-dimensional travel-time model and numerical acceptance gates. These solutions are reconnaissance results, not a replacement for manual P- and S-phase review, station corrections, a validated three-dimensional velocity model, or double-difference relocation. First-motion focal mechanisms were screened by polarity misfit and station-gap criteria; no mechanism was accepted for the ML 3.2 Adalar event.

3.3 Spatial statistics and uncertainty

Event density was evaluated on a 5-km grid. Candidate spatial neighborhoods were compared using standardized permutation results for Global Moran's I. Local Getis–Ord Gi* values were then calculated at the selected distance and adjusted for multiple tests using the Benjamini–Hochberg false-discovery-rate procedure. Unweighted and magnitude/depth-weighted standard deviational ellipses summarize spatial dispersion. Bootstrap resampling was used to describe uncertainty in ellipse orientation. These statistics describe the observed catalog; they are not probabilities of future epicentres or rupture dimensions.

3.4 Stress and engineering screening

The Coulomb calculation represents the 23 April 2025 Mw 6.2 source as a static double-couple point source in a homogeneous elastic full space. Receiver geometry follows the nearest mapped Marmara fault segment, and the unreliable rupture core is masked. The calculation tests the sign and sensitivity of regional stress transfer; it is not a finite-fault triggering model. Engineering-geological interpretation was synthesized from indexed site-response, velocity-structure, strong-motion, and regional hazard studies. No borehole, CPT, SPT, groundwater, or laboratory soil dataset was available, so no site-specific design or liquefaction conclusion is made.

4. Results and geophysical interpretation of Figures S2–S11

4.1 Catalog development and magnitude information—Figure S2

Figure S2 shows that the most important change in the catalog is temporal concentration. Regional activity was present throughout the study period, but Adalar activity rose strongly on 19 and 20 August. The cumulative curve becomes steep after the ML 3.2 event. The magnitude histogram is dominated by small earthquakes. This is expected for tectonic catalogs and is consistent with a b-value near 1.14 above the estimated completeness magnitude Mc=2.95. A b-value near one is common and is not a stand-alone earthquake precursor (Aki, 1965).

The cross-agency panel shows generally small magnitude differences, commonly 0.0–0.2 units. This supports the reconciliation procedure but does not make all magnitudes identical. Magnitude type, station coverage and agency processing can change the reported value. The final 20 August count is incomplete after 10:18:27 UTC, so daily comparisons must retain this cutoff.

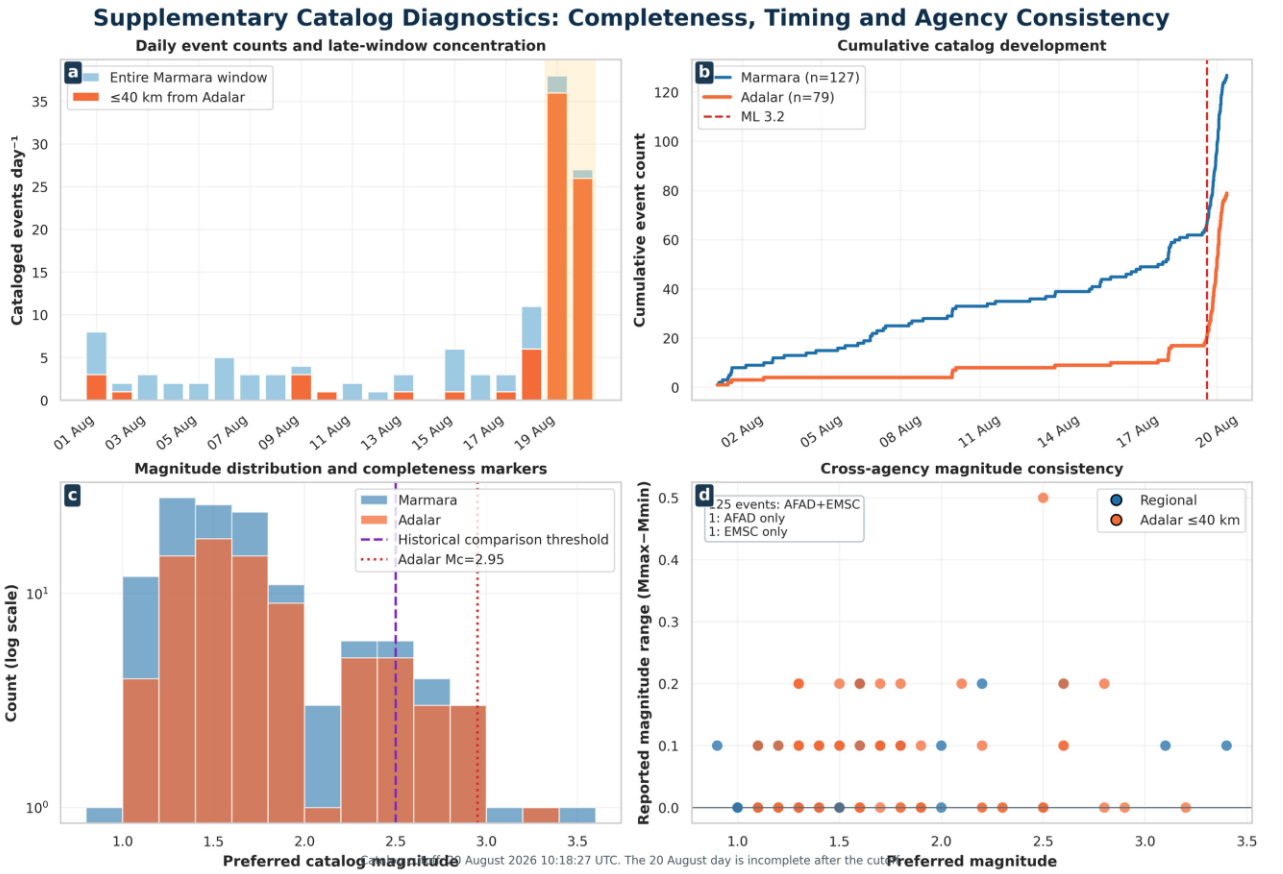

Figure S2. Temporal and magnitude diagnostics of the reconciled Marmara and Adalar catalogs. The late-window rise is real in the supplied catalog, but the final day is incomplete and agency solutions may be revised.

4.2 Space–time behavior of the Adalar sequence—Figure S3

Figure S3 maps the 79 Adalar-window events and colors them by time after 18 August. The recent events form a compact group south of the islands. The main catalog axis is approximately 31° from north. This value describes the shape of the point cloud; it is not automatically the strike of the active fault and it is not a stress direction.

The inter-event-time plot shows strong temporal compression on 19–20 August. Shorter inter-event times indicate clustering, but clustering can occur during ordinary aftershock or swarm-like processes. Without precise relative locations, focal mechanisms, fluid-pressure observations or a larger following event, the sequence cannot be classified as a preparatory rupture process.

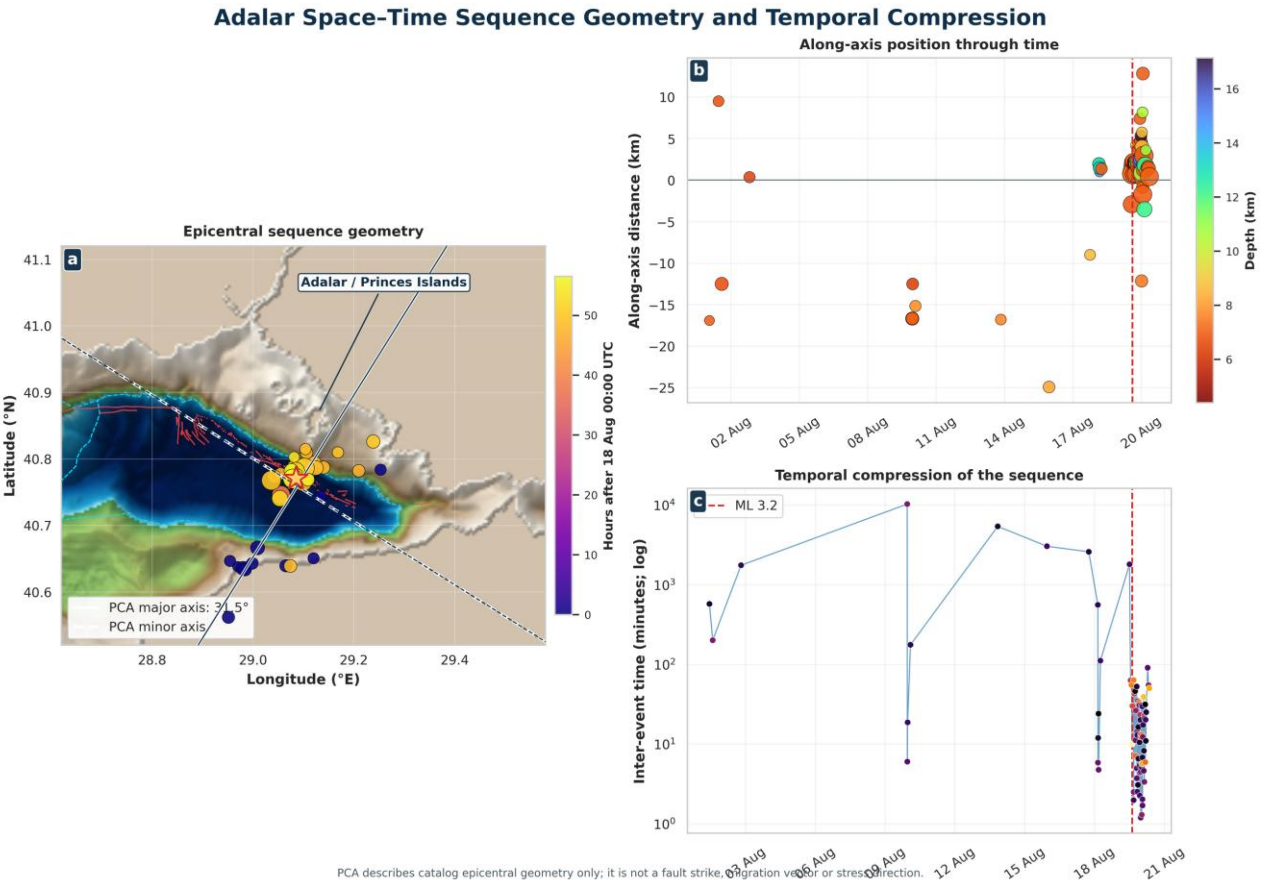

Figure S3. Adalar sequence geometry, along-axis development and inter-event-time compression. PCA is used only as a descriptive axis and does not define a future rupture direction.

4.3 Geostatistical clustering and robustness—Figures S4 and S5

Figure S4 tests several spatial neighborhoods. The 10-km model produced the largest standardized Moran result, with z=21.69. This indicates that the mapped distribution is more clustered than expected under the stated randomization. Local Getis–Ord analysis identified 13 hot cells at the 99% level and one at the 95% level after Benjamini–Hochberg false-discovery-rate correction (Getis & Ord, 1992; Benjamini & Hochberg, 1995).

Statistical significance does not mean geological certainty. Hot cells depend on the event catalog, the 5-km grid and the 10-km binary neighborhood. The hotspot map is useful for comparing local event density and for placing instruments. It must not be published as a probability map of the next earthquake.

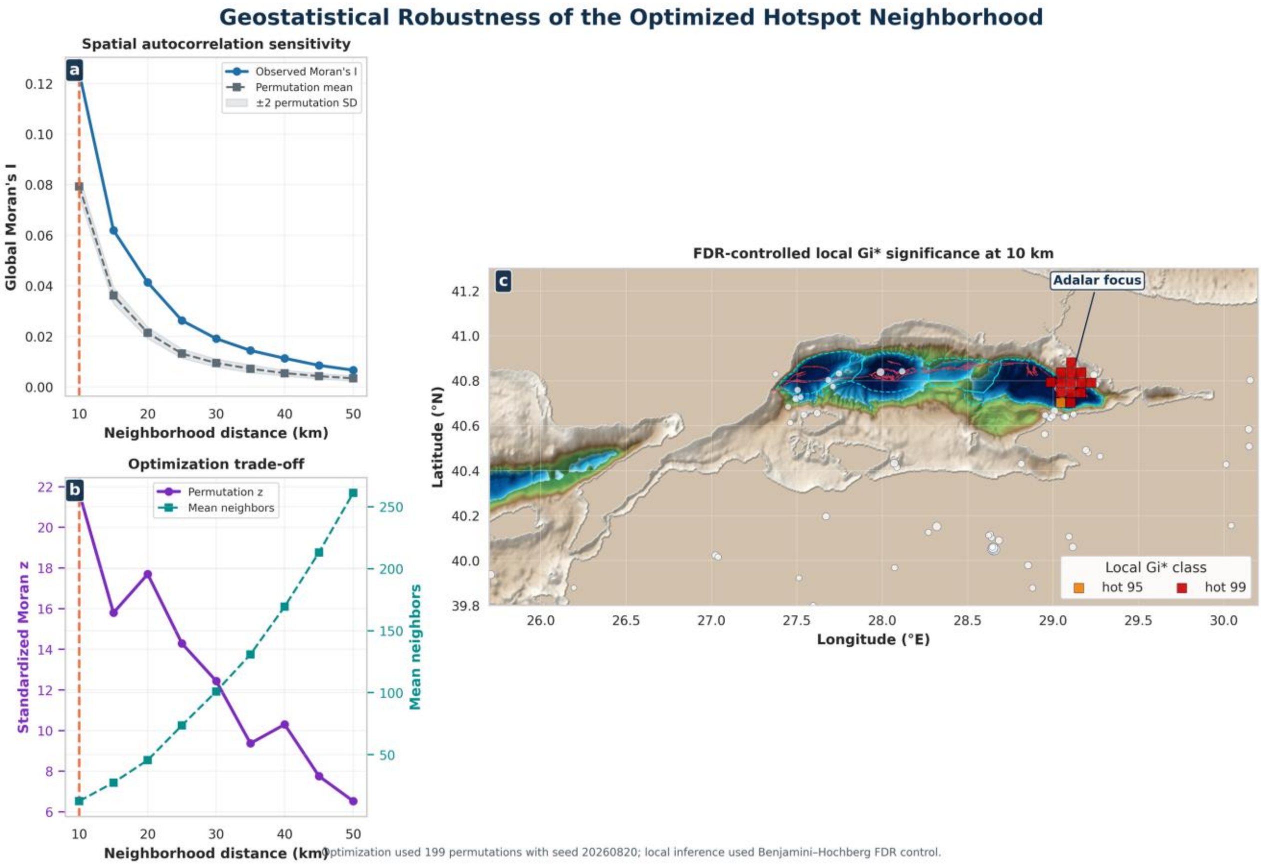

Figure S4. Sensitivity of Global Moran's I and the FDR-controlled local Gi* classification. The 10-km neighborhood is the optimized scale for this catalog and grid.

Figure S5 adds bootstrap uncertainty to the standard deviational ellipses. The unweighted long-axis azimuth has a 95% bootstrap range of about 67.4–81.7°, while the magnitude/depth-weighted result is broader, about 39.4–73.7°. The weighted ellipse shifts eastward because larger and shallower events receive greater visualization weight. The bootstrap clouds show that center and orientation are not exact.

These ellipses summarize regional spatial dispersion. They do not represent fault rupture length, a confidence region for a future epicenter or an engineering hazard zone. Their correct use is comparison between datasets and evaluation of spatial stability.

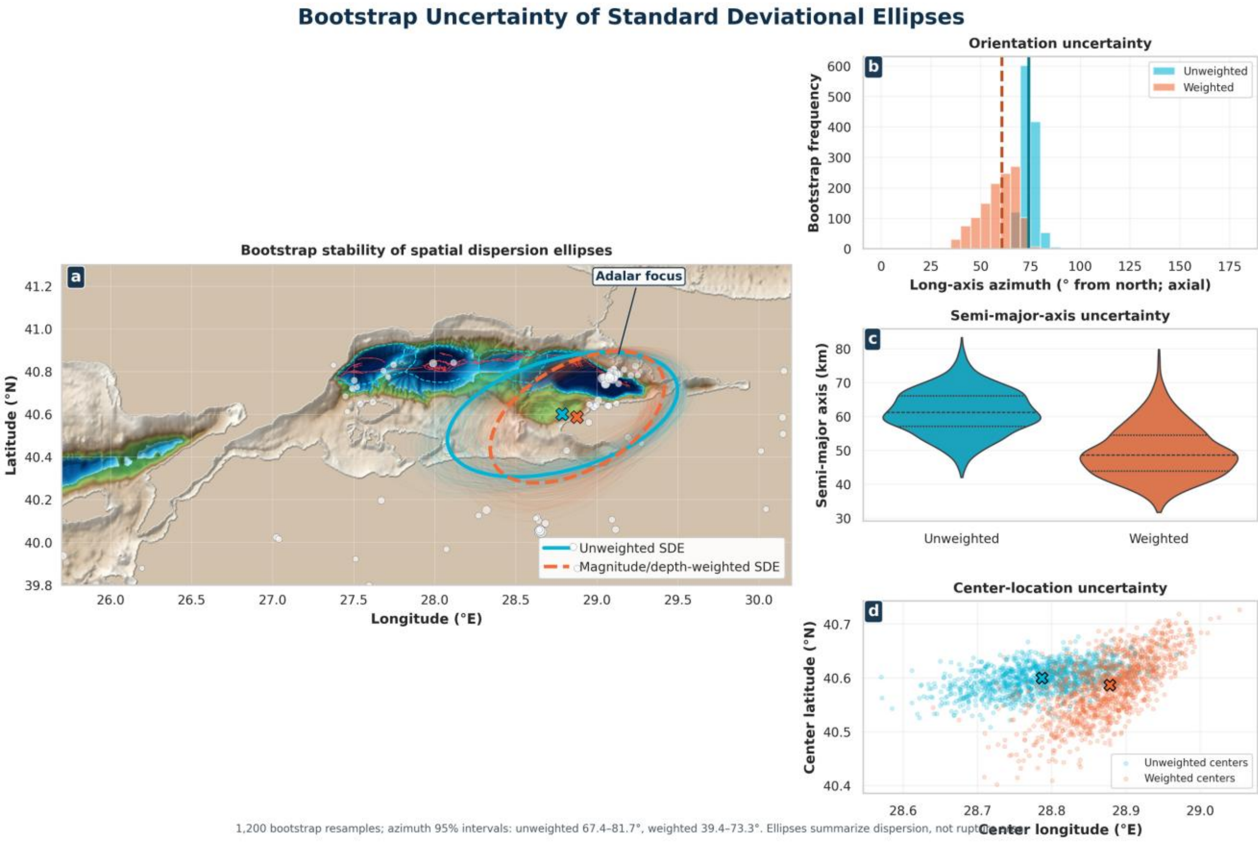

Figure S5. Bootstrap uncertainty of unweighted and magnitude/depth-weighted SDEs. The ellipses describe catalog dispersion and are not rupture areas.

4.4 Depth structure and 3D geometry—Figures S6 and S10

Figure S6 presents two orthogonal depth sections through the Adalar event cloud. Most events are reported between about 6 and 9 km, with some deeper events near 15–16 km. A strong vertical concentration at approximately 7 km is visible. However, many agency catalogs use similar nominal depths when depth is weakly resolved. It would be unsafe to interpret this feature as a real horizontal seismic layer without reviewed phases and a three-dimensional velocity model.

Figure S10 shows the same events in three dimensions with seafloor relief and projected side views. It is useful for understanding the source volume and its relation to mapped structures. It also makes the depth limitation visible: the points are precise symbols, but their true uncertainty is larger than the symbols. The figure should be used for conceptual geometry, not exact fault-to-foundation distance.

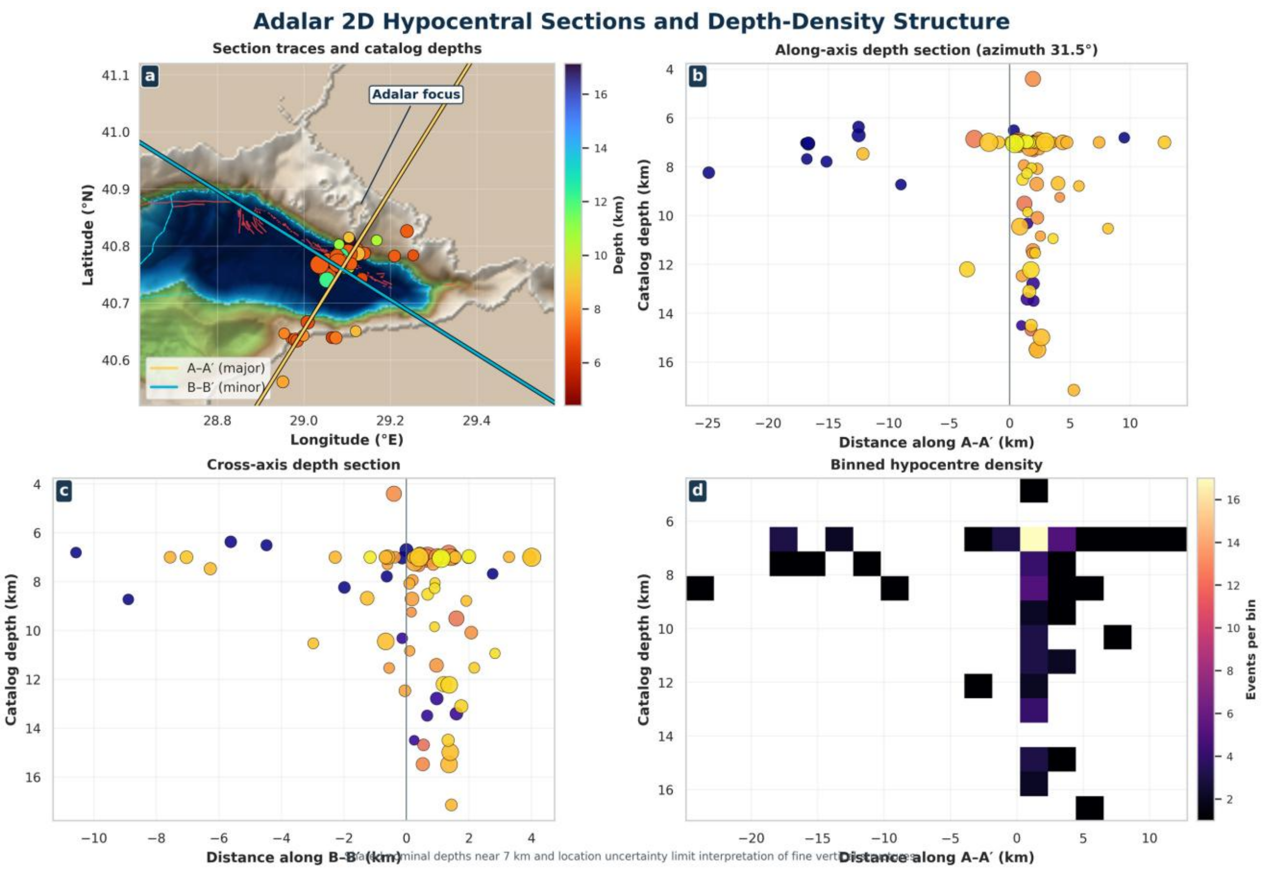

Figure S6. Orthogonal Adalar depth sections and binned hypocentre density. Fine vertical structures are not interpreted because catalog depth uncertainty is substantial.

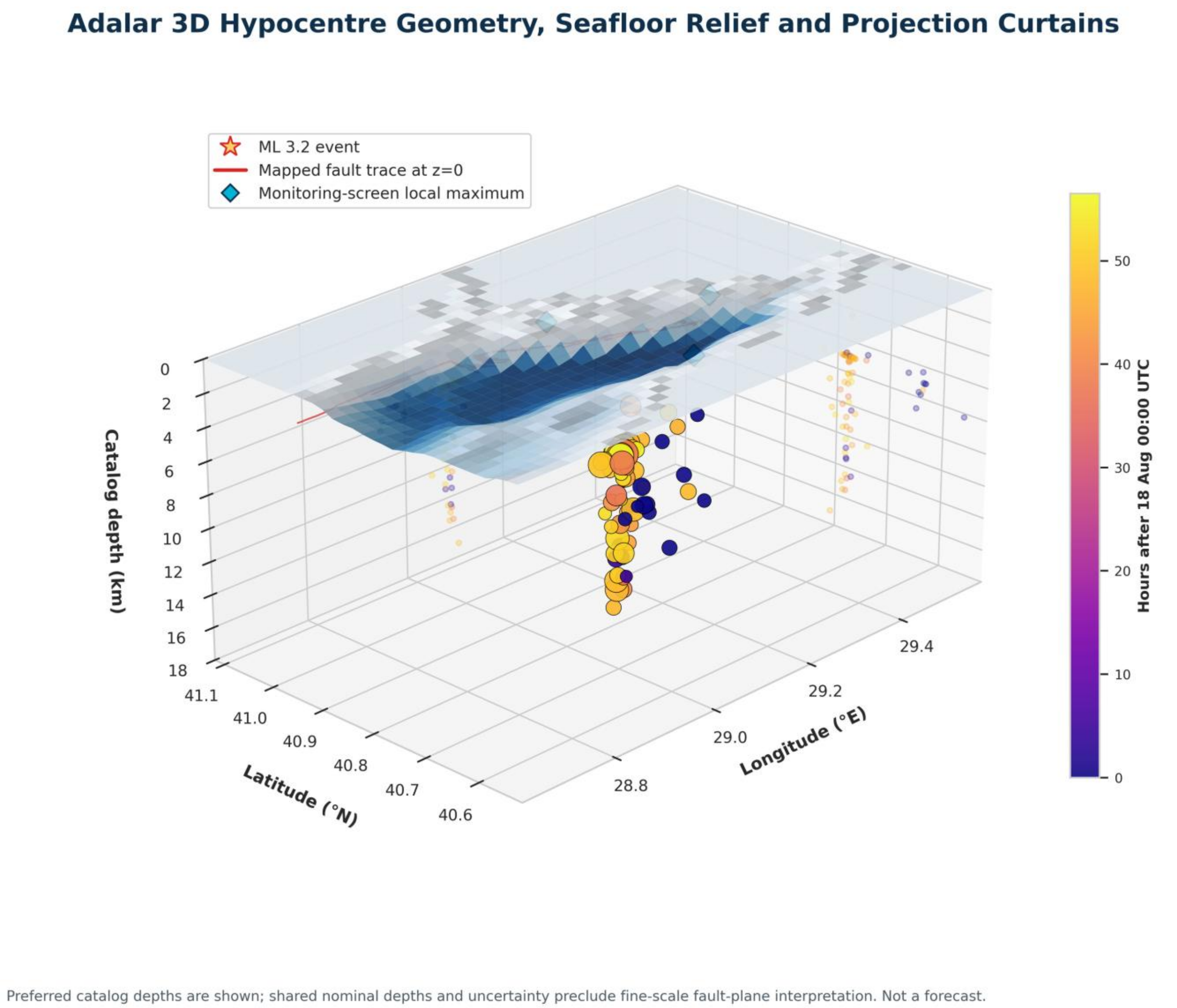

Figure S10. Three-dimensional Adalar hypocentre geometry with seafloor relief and projection curtains. Preferred catalog depths are shown; this is not a definitive fault plane.

4.5 Station geometry, picks and relocation quality—Figures S7 and S8

Figure S7 shows that the waveform archive is valuable but not balanced. The analysis used 549 automatic P picks from 49 stations, but 547 came from the KO network. The median signal-to-noise ratio is 5.83 and the median pick uncertainty is about 0.060 s. For the ML 3.2 Adalar event, only four automatic P picks were retained. This is not enough for a robust offshore hypocentre or double-couple mechanism under the present workflow.

Figure S8 confirms the effect of station geometry. Twelve of 22 trial relocations passed the notebook's permissive gates, but the median accepted depth uncertainty is about 17.9 km. Only four solutions have both horizontal and depth uncertainty at or below 10 km. A low travel-time residual does not guarantee a well-resolved depth. Offshore location should therefore be improved with analyst-picked phases, station corrections, ocean-bottom or island stations, and double-difference methods.

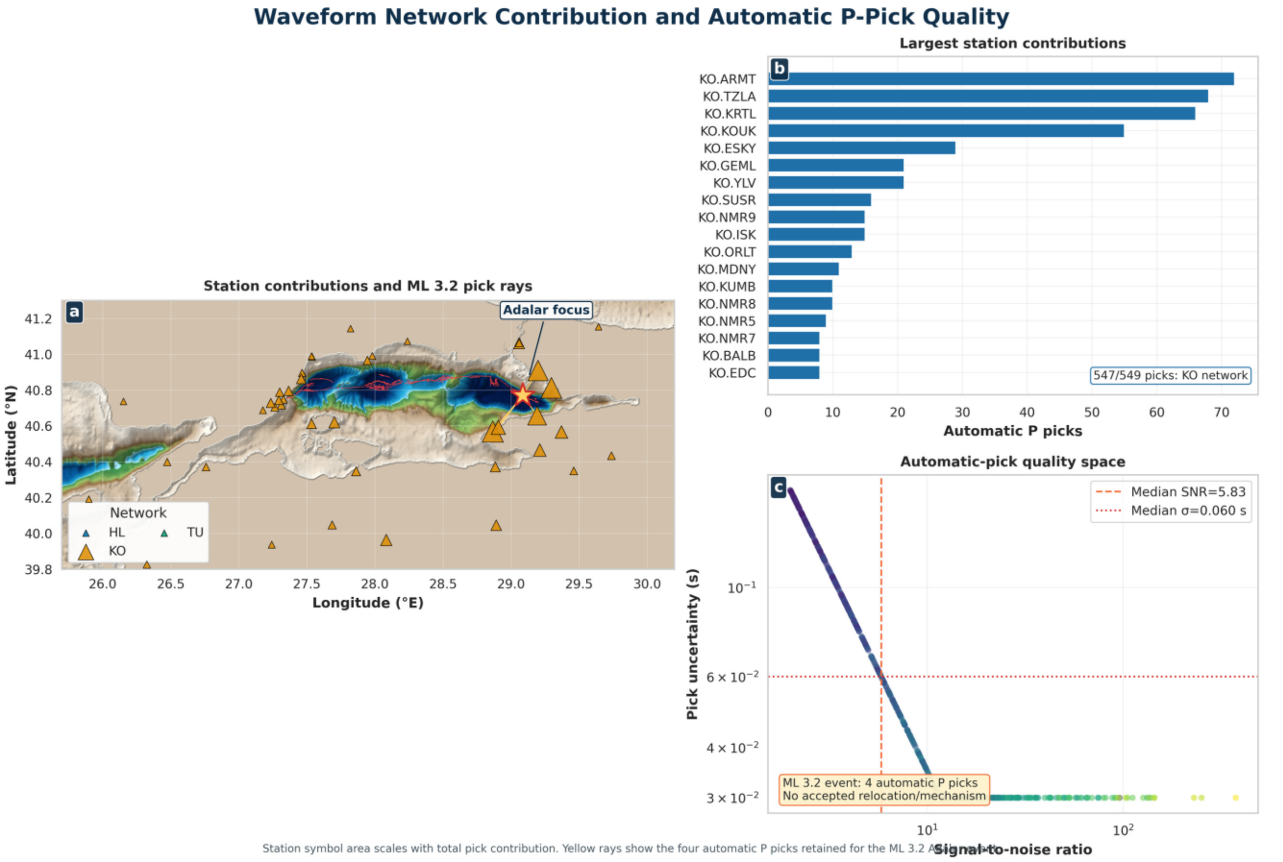

Figure S7. Station contributions and automatic P-pick quality. The KO network dominates, and the ML 3.2 event has only four retained automatic P picks.

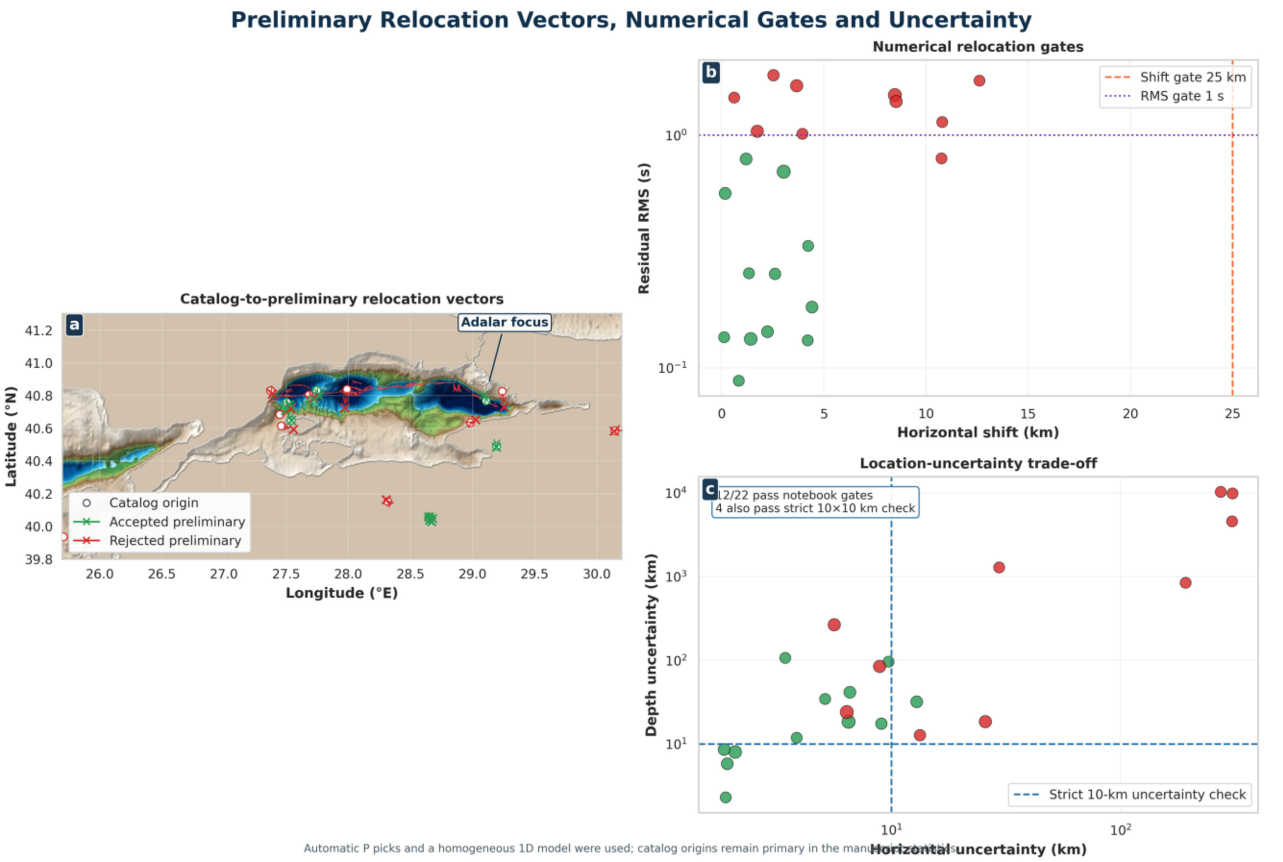

Figure S8. Trial relocation vectors, numerical gates and uncertainty. Twelve solutions pass permissive gates; only four pass the stricter 10-km horizontal and depth uncertainty check.

4.6 Focal mechanisms and stress direction—Figure S9

Figure S9 includes nine accepted coarse first-motion mechanisms and one withheld solution. Their median polarity misfit is low, but the mechanisms are spatially uneven and their P-axis directions are widely dispersed. The axial resultant R≈0.20 confirms that the mean direction is weak. Most accepted mechanisms come from western or terrestrial parts of the study area, not the late Adalar cluster.

For this reason, the regional maximum compression near N35°E from published stress inversion remains the more reliable first-order direction (Wollin et al., 2019). Local stress can rotate around basin margins, fault bends and normal-fault components. A new Adalar stress inversion requires more reviewed mechanisms distributed around the eastern basin.

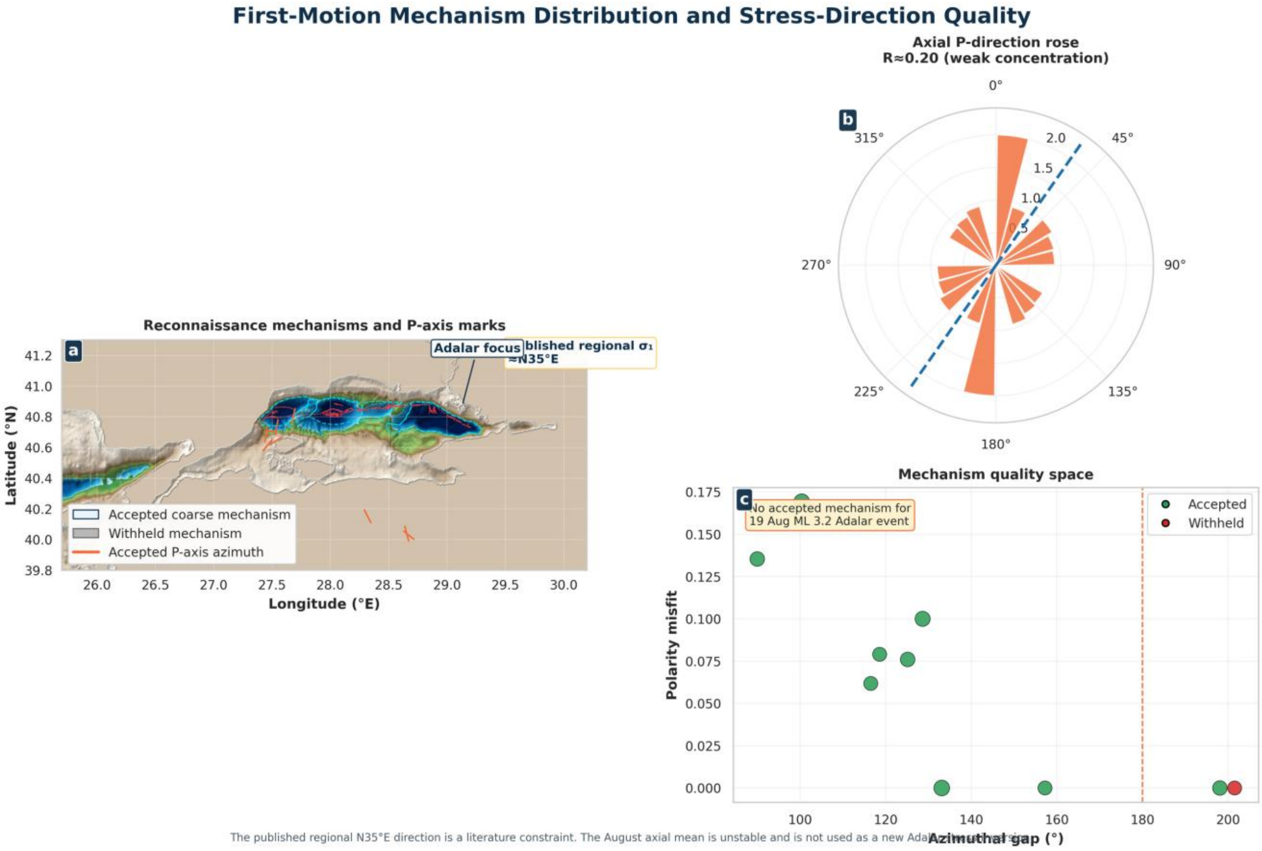

Figure S9. Reconnaissance focal mechanisms, axial P-direction statistics and mechanism-quality space. The August mechanism set is insufficient for a new Adalar stress tensor.

4.7 Coulomb stress screening—Figure S11

Figure S11 summarizes a point-source Coulomb calculation for the 23 April 2025 Mw 6.2 earthquake. The Çınarcık receiver corridor has a median ΔCFS of +0.204 kPa, and 72.5% of its cells are positive under the selected receiver geometry. Positive ΔCFS means that the assumed slip sense is slightly promoted; negative values mean that it is inhibited. The sign depends on source and receiver orientation (King et al., 1994).

The median Adalar-side value is only 0.000204 MPa. This is very small compared with the commonly used order-of-magnitude screening level of 0.01 MPa. Large tails in some near-source corridors are caused by the point-source approximation and are highly sensitive to geometry and distance. The 2025 earthquake should therefore not be described as the demonstrated trigger of the August 2026 sequence. A reviewed finite-fault model, afterslip, poroelastic and viscoelastic tests are required.

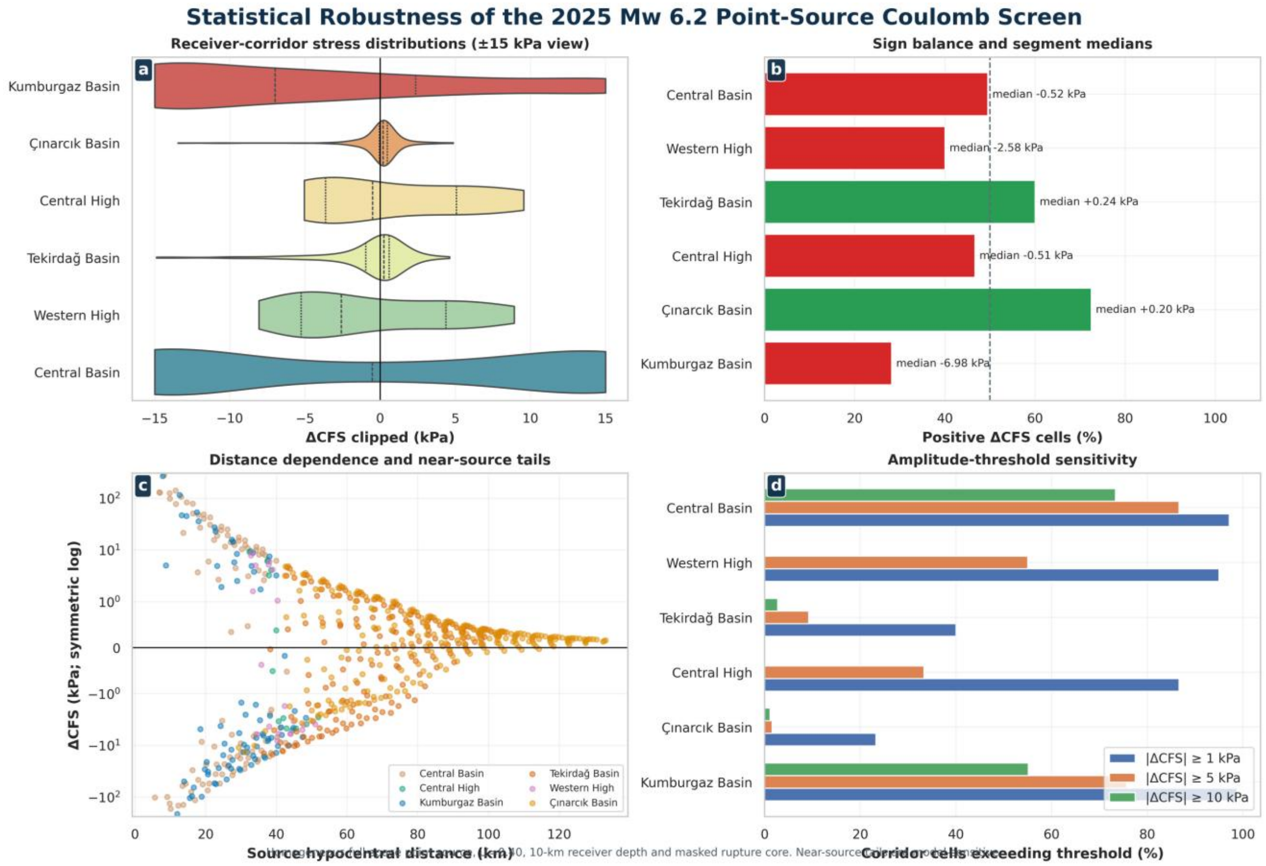

Figure S11. Segment-level distributions, sign balance, distance dependence and threshold sensitivity of the 2025 point-source Coulomb screen. The result is model dependent and not a forecast.

5. Engineering-geological and geotechnical interpretation

5.1 Source information versus site information

The supplementary figures mainly describe the earthquake source region. Geotechnical response occurs at the site. These are linked, but they are not the same. Source magnitude, depth, rupture direction and distance control the incoming seismic waves. Local geology, sediment thickness, shear-wave velocity, damping, groundwater, topography and foundation conditions control how those waves affect the ground and structures.

This distinction is important for Adalar and İstanbul. The Çınarcık Basin and the coastal margins contain thick sediments and sharp geological boundaries. Three-dimensional ground-motion simulations show that source complexity and basin structure can strongly change shaking across İstanbul (Infantino et al., 2020). Earlier scenario studies also found strong sensitivity to source and propagation parameters (Pulido et al., 2004). The August cluster improves source monitoring but does not replace site-response mapping.

5.2 Site amplification and resonance

Published observations demonstrate local amplification in İstanbul. Ergin et al. (2004) measured important site amplification at Avcılar. Karabulut and Özel (2018) used microtremor arrays to construct three-dimensional shear-wave velocity models on the European side. Keskinsezer et al. (2023) combined MASW and HVSR measurements near Maltepe and the Marmara coast. They identified low Vs30, higher dominant period and higher vulnerability indicators in coastal alluvial and deltaic materials compared with more competent higher ground.

The engineering implication is that two sites at similar distance from the offshore fault may experience different shaking. Thick soft deposits may amplify long-period motion, while shallow impedance contrasts can increase short-period motion. Basin edges may produce complex two-dimensional or three-dimensional effects. Building period must therefore be compared with measured site period, not inferred from the earthquake map alone.

5.3 Liquefaction, settlement and lateral spreading

Low-lying coastal fills, young alluvium and saturated deltaic deposits can be susceptible to cyclic pore-pressure increase. However, no liquefaction conclusion can be obtained from Figures S2–S11. A valid assessment requires groundwater depth, grain-size distribution, density, fines content, SPT or CPT resistance, stress history and a design ground-motion level. The present results can only identify the need to investigate coastal areas where soft sediments and high exposure occur.

The same limitation applies to settlement and lateral spreading. These require soil stratigraphy, compressibility, cyclic strain and slope or shoreline geometry. A hot earthquake cell offshore is not a liquefaction map on land.

5.4 Slopes, submarine sediments and lifelines

Steep submarine basin margins and coastal slopes may respond to strong shaking through deformation or local instability. The 3D relief in Figure S10 is useful for identifying where future bathymetric and geotechnical profiles should be concentrated. It does not provide sediment strength, pore pressure or factor of safety. Submarine cables, pipelines, ports, coastal roads and ferry infrastructure need route-specific assessment that combines seismic shaking, fault displacement and slope stability.

5.5 Foundation and structural-design implications

The August sequence does not directly change foundation bearing capacity or settlement values. It does reinforce the importance of using current hazard scenarios and site-specific ground models. Engineering design requires code-compatible spectra, soil class, nonlinear site response where necessary, and structural analysis. The source screening maps may help select credible scenario directions, but they are not design spectra.

Table 2. Geotechnical implications and required evidence.

Issue	Screening implication	Required site data	Important limit
Site amplification	Possible in soft coastal/basin deposits	MASW, HVSR, borehole Vs, strong-motion records	Do not assign amplification from event density
Liquefaction	Potential concern in saturated loose fills/alluvium	CPT/SPT, groundwater, grading, density, cyclic demand	No liquefaction map is produced here
Settlement	Possible in compressible or loose deposits	Oedometer, CPT/SPT, modulus and layer thickness	Cannot be calculated from seismic catalog
Slope/submarine stability	Strong shaking may destabilize susceptible slopes	Bathymetry, seismic profiles, cores, strength and pore pressure	Relief alone is not factor of safety
Surface fault displacement	Relevant near mapped active traces	Detailed fault mapping, paleoseismology, geodesy	Hotspot score is not displacement probability
Foundation demand	Depends on site motion and structural period	Code spectrum, site response, foundation–soil model	Coulomb stress is not design acceleration

Note. *The table identifies investigation needs; it does not classify individual sites.*

6. Integrated multidisciplinary assessment

The figures show three different levels of information. First, the observation level is strong: a compact Adalar sequence occurred on 19–20 August and was recorded in a regional waveform archive. Second, the interpretation level is moderate: geostatistics show clustering, and regional tectonic studies support continuing concern about the eastern MMF. Third, the prediction level is not supported: the available data cannot specify the next event's time, magnitude or exact epicenter.

Geotechnically, the most important conclusion is spatial variability. İstanbul, Adalar and the Marmara coasts include competent rock, weathered rock, alluvium, deltaic deposits, fills and deep sedimentary basins. Source directivity and basin effects may combine to produce uneven shaking. This justifies integrated source–path–site modeling, not a single uniform hazard value.

Table 3. Evidence strength and next action.

Interpretation	Current confidence	Basis	Required improvement
Late Adalar sequence	High	Direct catalog observation	Continue near-real-time review
10-km clustering	High within stated model	Permutation and FDR controlled	Test other grids and declustering

Interpretation	Current confidence	Basis	Required improvement
Exact fault plane/depth	Low to moderate	Automatic picks and large depth uncertainty	3D/double-difference relocation
New Adalar stress direction	Low	Sparse, dispersed first motions	More reviewed mechanisms
Regional N35°E compression	Moderate to high	Published regional inversion	Allow local rotations
2025 triggering of Aug 2026 sequence	Low	Small point-source median ΔCFS	Finite-fault and transient sensitivity
Site amplification concern	Moderate to high regionally	Indexed MASW/HVSR and strong-motion studies	Site-specific measurements required
Liquefaction at a named site	Not assessed	No CPT/SPT or groundwater data	Dedicated geotechnical investigation

Note. *Confidence is qualitative and applies only to this report's stated evidence.*

7. Recommended investigations

1. Manually review P and S arrivals for the 19–20 August sequence and calculate consistent local magnitudes.
2. Relocate the sequence with a validated three-dimensional velocity model, station corrections and double-difference methods.
3. Expand eastern Marmara coverage using GONAF boreholes, island stations, ocean-bottom instruments and the Kartal–Adalar–Erenköy submarine DAS cable described by Kartal et al. (2026).
4. Repeat focal-mechanism analysis after polarity review and perform uncertainty-aware stress inversion only when the eastern event set is sufficiently distributed.
5. Replace the 2025 point source with reviewed finite-fault slip models and test effective friction, receiver geometry, depth, afterslip, poroelastic and viscoelastic processes.
6. Prepare a geotechnical database for Adalar and the İstanbul coastal belt containing boreholes, lithology, SPT/CPT, Vs30, groundwater, laboratory dynamic properties and foundation records.
7. Perform MASW/HVSR arrays and borehole measurements across rock–soil and basin-edge transitions; compare measured site periods with building periods.
8. Carry out liquefaction, settlement and lateral-spreading analyses only after site-specific subsurface and groundwater data are available.
9. Use nonlinear 1D/2D/3D site-response models and physics-based source scenarios for important lifelines, ports, hospitals, bridges and emergency infrastructure.
10. Maintain versioned, open metadata and clear public communication that separates observation, screening, hazard and prediction.

Table 4. Prioritized multidisciplinary work program.

Priority	Investigation	Main objective
Immediate	Phase review; sequence relocation; waveform QC	Resolve whether events occupy one structure or several
Immediate	Continuous DAS/borehole/island monitoring	Improve eastern offshore detection and timing
Short term	MASW, HVSR and borehole Vs profiles	Map site period, Vs30 and basin-edge variation
Short term	Groundwater and CPT/SPT program in coastal deposits	Screen liquefaction and settlement
Short term	Finite-fault Coulomb sensitivity	Test robustness of the small Çınarcık median
Medium term	3D source–path–site simulations	Estimate spatially variable strong motion
Medium term	Lifeline and submarine-slope assessment	Evaluate cascading coastal infrastructure hazards

Note. *Priority refers to information value and public-safety relevance, not a prediction of event timing.*

8. Conclusions

11. The 1–20 August 2026 catalog contains a clear late-window Adalar sequence: 62 of 79 Adalar-window events occurred on 19–20 August.
12. Geostatistical clustering is significant under the stated grid and 10-km neighborhood, but hotspot cells are not future-earthquake probabilities.
13. The source volume is centered mainly at nominal catalog depths near 7 km, but large depth uncertainty prevents detailed fault-plane interpretation.

14. Station and pick coverage are insufficient for a robust relocation or focal mechanism of the ML 3.2 Adalar event. The August mechanisms do not define a new stress tensor.
15. Published regional compression near N35°E and the documented locked–creeping MMF architecture remain the most defensible tectonic constraints.
16. The point-source 2025 Coulomb median in the Çınarcık corridor is positive but very small and cannot demonstrate triggering of the August sequence.
17. The geotechnical consequence is a need for integrated source–path–site analysis. Coastal and basin sediments may amplify shaking, but site-specific Vs, groundwater and resistance data are mandatory.
18. The combined evidence supports dense monitoring and detailed ground investigation; it does not support an earthquake prediction.

Final scientific statement
Figures S2–S11 provide a strong observational and screening framework for the Marmara–Adalar region. Engineering decisions must add site-specific geotechnical measurements, code-compatible hazard analysis and structural assessment.

9. Limitations and interpretation boundaries

1. Catalog and waveform services can revise origins, magnitudes and metadata after the cutoff.
2. The 20 August count is incomplete after 10:18:27 UTC.
3. Automatic picks and a homogeneous 1D relocation model are reconnaissance tools.
4. No accepted focal mechanism is available for the ML 3.2 Adalar event.
5. The relief source is the supplied local F7_2024 raster and requires formal archive, licence and citation before publication.
6. The monitoring score, hotspot map, SDE and Coulomb screen are not probabilistic seismic-hazard products.
7. No direct geotechnical field or laboratory data are included in this report.

10. Declarations

10.1 Author contribution

Shaheen Mohammed Saleh Ahmed: conceptualization, data curation, methodology, software, formal analysis, validation, visualization, interpretation, writing—original draft, and writing—review and editing.

10.2 Funding

This research received no specific grant from public, commercial, or not-for-profit funding agencies.

10.3 Competing interests

The author declares no competing financial or non-financial interests.

10.4 Data and code availability

Event origins and magnitudes were obtained from the public AFAD, EMSC, and USGS services; waveform and station metadata were obtained from contributing FDSN/EIDA providers. EarthArXiv accepts one manuscript PDF and does not directly host supplementary datasets. The reconciled catalog, analysis notebook, processed tables, and publication figures are available from the corresponding author on reasonable request while a persistent public data archive is prepared. Raw waveform ownership and reuse conditions remain with the originating data providers.

10.6 Ethics statement

This study uses earthquake catalogs, geophysical waveforms, geospatial products, and published literature. It involves no human participants, animals, or private personal data.

11. References

Aki, K. (1965). Maximum likelihood estimate of b in the formula log N = a − bM and its confidence limits. Bulletin of the Earthquake Research Institute, 43, 237–239.

Becker, D., Martínez-Garzón, P., Wollin, C., Kılıç, T., & Bohnhoff, M. (2023). Variation of fault creep along the overdue Istanbul–Marmara seismic gap in NW Türkiye. Geophysical Research Letters, 50(6), e2022GL101471. https://doi.org/10.1029/2022GL101471

Benjamini, Y., & Hochberg, Y. (1995). Controlling the false discovery rate: A practical and powerful approach to multiple testing. Journal of the Royal Statistical Society: Series B, 57(1), 289–300. https://doi.org/10.1111/j.2517-6161.1995.tb02031.x

Bohnhoff, M. (2026). Rethinking the Main Marmara Fault—seismotectonic complexity and seismic hazard in the Istanbul–Marmara region. Geophysical Journal International, 246(3), ggag253. https://doi.org/10.1093/gji/ggag253

Bohnhoff, M., Bulut, F., Dresen, G., Malin, P. E., Eken, T., & Aktar, M. (2013). An earthquake gap south of Istanbul. Nature Communications, 4, 1999. https://doi.org/10.1038/ncomms2999

Chen, X., Martínez-Garzón, P., Kwiatek, G., Ben-Zion, Y., Bohnhoff, M., & Cotton, F. (2025). Rupture directivity of moderate earthquakes along the Main Marmara Fault suggests larger ground motion towards Istanbul. Geophysical Research Letters, 52(1), e2024GL111460. https://doi.org/10.1029/2024GL111460

Erdik, M., Demircioğlu, M., Şeşetyan, K., Durukal, E., & Siyahi, B. (2004). Earthquake hazard in Marmara region, Turkey. Soil Dynamics and Earthquake Engineering, 24(8), 605–631. https://doi.org/10.1016/j.soildyn.2004.04.003

Ergin, M., Özalaybey, S., Aktar, M., & Yalçın, M. N. (2004). Site amplification at Avcılar, Istanbul. Tectonophysics, 391(1–4), 335–346. https://doi.org/10.1016/j.tecto.2004.07.021

Ergintav, S., Reilinger, R. E., Çakmak, R., Floyd, M., Çakir, Z., Doğan, U., King, R. W., McClusky, S., & Özener, H. (2014). Istanbul's earthquake hot spots: Geodetic constraints on strain accumulation along faults in the Marmara seismic gap. Geophysical Research Letters, 41(16), 5783–5788. https://doi.org/10.1002/2014GL060985

Fernandez, N., Cacace, M., & Scheck-Wenderoth, M. (2026). The role of crustal rheology and mantle fluids on the interseismic behavior of the Main Marmara Fault. Journal of Geophysical Research: Solid Earth, e2025JB032574. https://doi.org/10.1029/2025JB032574

Getis, A., & Ord, J. K. (1992). The analysis of spatial association by use of distance statistics. Geographical Analysis, 24(3), 189–206. https://doi.org/10.1111/j.1538-4632.1992.tb00261.x

Güvercin, S. E., & Barbot, S. (2025). Persistent rupture segmentation of the Main Marmara Fault. Communications Earth & Environment, 6, 1028. https://doi.org/10.1038/s43247-025-03007-4

Infantino, M., Mazzieri, I., Özcebe, A. G., Paolucci, R., & Stupazzini, M. (2020). 3D physics-based numerical simulations of ground motion in Istanbul from earthquakes along the Marmara segment of the North Anatolian Fault. Bulletin of the Seismological Society of America, 110(5), 2559–2576. https://doi.org/10.1785/0120190235

Karabulut, S., & Özel, O. (2018). 3-D shear wave velocity structure beneath the European Side of Istanbul from seismic noise arrays analysis. Geophysical Journal International, 215(3), 1803–1823. https://doi.org/10.1093/gji/ggy370

Kartal, R. F., Kadirioğlu, F. T., Kılıç, T., Rodríguez Tribaldos, V., Martínez-Garzón, P., Bohnhoff, M., Hillmann, L., & Krawczyk, C. M. (2026). Distributed acoustic sensing observations of the 2025 April 23 Mw 6.2 Marmara earthquake in Northwestern Türkiye and its comparison with borehole seismometer data. Geophysical Journal International, 246(2), ggag203. https://doi.org/10.1093/gji/ggag203

Keskinsezer, A., Karaaslan, H., Silahtar, A., & Beyhan, G. (2023). The soil characterization of the region between the Maltepe–Beykoz Fault and the Marmara Sea in İstanbul (Türkiye) with the integrated HVSR and MASW method. Journal of Applied Geophysics, 219, 105245. https://doi.org/10.1016/j.jappgeo.2023.105245

King, G. C. P., Stein, R. S., & Lin, J. (1994). Static stress changes and the triggering of earthquakes. Bulletin of the Seismological Society of America, 84(3), 935–953.

Korkusuz Öztürk, Y., Konca, A. Ö., & Özel, N. M. (2025). 3D dynamic rupture simulations for the potential Main Marmara Fault earthquake in the Sea of Marmara based on inter-seismic strain accumulation. Journal of Geophysical Research: Solid Earth, 130(7), e2024JB029585. https://doi.org/10.1029/2024JB029585

Lange, D., Kopp, H., Royer, J.-Y., Henry, P., Çakir, Z., Petersen, F., Sakic, P., Ballu, V., Bialas, J., Özeren, M. S., Ergintav, S., & Géli, L. (2019). Interseismic strain build-up on the submarine North Anatolian Fault offshore Istanbul. Nature Communications, 10, 3006. https://doi.org/10.1038/s41467-019-11016-z

Le Pichon, X., Şengör, A. M. C., Demirbağ, E., Rangin, C., İmren, C., Armijo, R., Görür, N., Çağatay, N., Mercier de Lépinay, B., Meyer, B., Saatçılar, R., & Tok, B. (2001). The active Main Marmara Fault. Earth and Planetary Science Letters, 192(4), 595–616. https://doi.org/10.1016/S0012-821X(01)00449-6

Martínez-Garzón, P., Chen, X., Becker, D., Núñez-Jara, S., Kartal, R. F., Türker, E., Dresen, G., Ben-Zion, Y., Jara, J., Cotton, F., Kadirioğlu, F. T., Kılıç, T., & Bohnhoff, M. (2026). Progressive eastward rupture of the Main Marmara fault toward Istanbul. Science, 391(6783), 379–383. https://doi.org/10.1126/science.adz0072

Pulido, N., Ojeda, A., Atakan, K., & Kubo, T. (2004). Strong ground motion estimation in the Sea of Marmara region (Turkey) based on a scenario earthquake. Tectonophysics, 391(1–4), 357–374. https://doi.org/10.1016/j.tecto.2004.07.023

Wollin, C., Bohnhoff, M., Vavryčuk, V., & Martínez-Garzón, P. (2019). Stress inversion of regional seismicity in the Sea of Marmara region, Turkey. Pure and Applied Geophysics, 176(3), 1269–1291. https://doi.org/10.1007/s00024-018-1971-1

Yamamoto, R., Kido, M., Ohta, Y., Takahashi, N., Yamamoto, Y., Pinar, A., Kalafat, D., Özener, H., & Kaneda, Y. (2019). Seafloor geodesy revealed partial creep of the North Anatolian Fault submerged in the Sea of Marmara. Geophysical Research Letters, 46(3), 1268–1275. https://doi.org/10.1029/2018GL080984